RESEARCH PAPER

Design and Optimization of Corrosion Behavior of Mg-Zn-Ca Alloy System Using Thermodynamic and Statistical Simulation

Mohsen Ghasvari[1], Mohammad Reza Aboutalebi[1,*], Ali Zamanian[2], Maryam Tajabadi[1]

* *mrezab@iust.ac.ir*

[1] School of Metallurgy and Materials Engineering, Iran University of Science and Technology (IUST) 16846-13114, Tehran, Iran

[2] Department of Nanotechnology and Advanced Materials, Materials and Energy Research Center, Karaj, Iran

Received: April 2026 **Revised: June 2026** **Accepted: July 2026**

DOI: 10.22068/ijmse.4603

Abstract: *In recent years, Mg-based alloys have been considered as a biodegradable biomaterial for implant applications. However, the high corrosion rate and hydrogen gas evolution in an aqueous environment are the most important challenges for these alloys. This study has focused on optimizing the biocorrosion properties of bioalloys in the Mg-Zn-Ca system, using an integrated approach of thermodynamic simulations and response surface methodology (RSM). It is believed that, in the Mg-Zn-Ca alloy system, the Mg_2Ca secondary phase usually enhances corrosion rate with microgalvanic coupling mechanisms. The ternary phases $Ca_xMg_yZn_z$ have less detrimental effects on corrosion resistance. To minimize the formation of deleterious phases, thermodynamic calculations were performed using CompuTherm's PANDAT software, and the predicted phase evolution was subsequently validated against experimental measurements. Corrosion behavior was assessed through potentiodynamic polarization tests and long-term immersion experiments. Based on the thermodynamic predictions, a statistical model was developed to guide the design of alloys with minimized detrimental secondary phases. The results showed that ZX31 (Mg-2.6Zn-1Ca) exhibited the highest corrosion potential (-1.6336 $V_{Ag/AgCl}$) and the lowest corrosion current density (216 $\mu A/cm^2$), showing higher biocorrosion resistance compared to ZX24 (Mg-2.3Zn-4.0Ca) and ZX15 (Mg-1.3Zn-4.8Ca).*

Keywords: *Magnesium bioalloy, Orthopedic implants, Biocorrosion, Corrosion optimization, Response surface methodology (RSM).*

1. INTRODUCTION

In recent decades, extensive research has been conducted on temporary orthopedic implants. Recent advances in materials science and engineering have played a significant role in improving the performance and biocompatibility of these devices. Current orthopedic implants are not only required to provide mechanical support, but also inevitably have properties such as bone regeneration, tissue engineering, drug delivery, and biodegradability [1–3]. The unique compatibility of metals such as magnesium (Mg), zinc (Zn), and calcium (Ca) with human metabolism, their favorable mechanical properties, and their safe degradation in the body highlight their interest as materials for bone implants [4, 5]. A temporary Mg implant should have properties such as appropriate biocompatibility, a degradation rate proportional to the tissue repair rate, and sufficient mechanical strength and integrity based on its functional needs [6-11]. However, one of the main issues of Mg-based biodegradable implants is uncontrollable corrosion in the biological environment. This issue may result in premature failure or insufficient strength of the new regenerated bone [12]. Mg alloys are susceptible to significant degradation in humid environments. Impurities such as iron (Fe) and nickel (Ni) can promote corrosion [13]. Ion concentration, pH value, and the presence of protein also increase the corrosion rate. The corrosion reaction of Mg produces hydrogen gas, especially in chloride-rich environments. This phenomenon leads to the formation of bubbles, which can be trapped in tissue. The H_2 bubble accumulation causes tissue necrosis and arterial occlusion if the bubbles enter the bloodstream. The corrosion rate reduction of Mg implants leads to reduced hydrogen gas release, which can be achieved by alloying, coating, and composite making [14-16].

The ternary alloy system Mg-Zn-Ca has a primary α-Mg matrix phase with limited solubility of Zn and Ca. Adding Zn up to 5 wt% reduces corrosion rate and hydrogen gas evolution around the implant [17]. However, excessive Zn can lead to neurotoxicity by forming the $ZnCl_2$ phase that impairs bone growth [18, 19]. The solubility limit of Ca in solid Mg is about 1.34 wt%, and excess Ca leads to the formation of Mg_2Ca precipitates at the grain boundaries that reduce corrosion resistance; thus,

[DOI: 10.22068/ijmse.4603]

the Ca level must be carefully controlled [17]. However, quaternary alloys exhibit reduced pitting corrosion due to improved eutectic secondary phases [20]. Research has shown that Mg-1Ca implants support osteogenesis without causing toxicity [21]. The Zn/Ca ratio is an important parameter that affects the formation of various intermetallic phases, including Mg_2Ca and $Ca_2Mg_6Zn_3$ [18]. Researchers have identified several key phases of the $Ca_xMg_yZn_z$ family, such as -$Ca_2Mg_6Zn_3$, -$Ca_2Mg_5Zn_{13}$, and $Ca_2Mg_5Zn_5$, which have similar properties [22-24]. Low Ca combined with optimized Zn enhances mechanical properties and corrosion resistance [25]. Zhang and Yang [26] showed that Ca amounts less than 0.5 wt% reduced the grain size; also, lower Zn/Ca ratios resulted in discontinuous eutectic phases that negatively affected the mechanical properties. Conversely, higher ratios promote continuous eutectic. Du et al. [27] noted that the presence of the $Ca_2Mg_6Zn_3$ phase enhances the corrosion resistance of Mg-3Ca alloys.

Despite the extensive research conducted on Mg alloys, particularly the ZX series, there is still a significant lack of comprehensive studies on the interactions among alloying elements. Most studies have focused on one or more specific alloys, building their conclusions by combining new findings with existing knowledge. Current methods commonly rely on the principle of Gibbs free energy minimization to determine the formation of stable and metastable phases [28]. As the range of new biomaterials continues to expand, the rapid and cost-effective selection of optimal materials becomes increasingly critical. Advanced computational tools capable of multi-criteria design offer a significant advantage in this regard, enabling broad material screening at minimal cost. Among these, software-based approaches stand out for their ability to evaluate a wide range of Mg alloy systems efficiently. The CompuTherm's PANDAT software database is particularly well-suited for this purpose, as it combines four essential characteristics: accuracy, physical realism, reliability, and safe extrapolation capability [29]. Several studies have employed these tools, including the work of Ghorbani et al. [30] to predict thermodynamic and mechanical properties; as well as the study performed by Morgenthal et al. [31] to estimate the appropriate sintering temperature, and some other studies to evaluate forming phases and phase diagrams [32-37]. Proposing a systematic framework for optimization problems of a wide range of alloys is more understandable than ever before. The primary objective of this study is to address this gap in the literature by employing thermodynamic and statistical models to systematically investigate novel magnesium bio-alloys rapidly and cost-effectively.

The novelty of this work resides in the development of a systematic, integrated computational-experimental framework for optimizing biocorrosion resistance in the Mg-Zn-Ca ternary alloy system. This approach couples thermodynamic phase prediction via CompuTherm's PANDAT software with response surface methodology (RSM) as a statistical optimization tool followed by experimental validation, enabling rapid, cost-effective screening and multi-criteria design of alloy compositions.

2. EXPERIMENTAL PROCEDURES

2.1. Methodology

This study presents a framework for database-driven alloy design, coupled with corrosion behavior prediction and optimization using RSM. For this purpose, firstly, the CompuTherm's PANDAT software and the new PanEvolution module (an extension of the previous PanPrecipitation) were employed to predict the phase fractions formed during processing of ZX-series Mg-alloys. The data obtained from the validated thermodynamic model were subsequently used to design and optimize the corrosion behavior of the alloys through RSM-based statistical modelling. Finally, the RSM predictions were experimentally validated through corrosion testing.

2.1.1. Secondary phases formation prediction

Among Mg alloying elements, Zn and Ca exhibit high biocompatibility. Due to the significant influence of Mg_2Ca and $Ca_xMg_yZn_z$ precipitates on the corrosion behavior of the alloy, the alloy range Mg-(1-7)Zn-(1-5)Ca was selected for corrosion behavior optimization.

To predict the formation of phases, the weight percentages of alloying elements Zn and Ca were considered as input data, and the weight percentages of α-Mg, Mg_2Ca, and $Ca_xMg_yZn_z$ phases were treated as outputs. CompuTherm's PANDAT software uses solid-state diffusion models to predict phase formation under non-equilibrium conditions (Scheil model). In the non-equilibrium model, rapid solidification is assumed without sufficient atomic motion in the solid state. Using diagrams similar to Figure 1, the volume fractions of all predicted phases were extracted at room temperature for the entire

[DOI: 10.22068/ijmse.4603]

investigated compositional range, and subsequently employed as a quantitative basis for alloy simulation and optimization. The predictable solid phases for this alloy range in the CompuTherm database include Mg-α, Mg_2Ca, $Ca_2Mg_5Zn_5$, $Ca_2Mg_5Zn_{13}$, and $Ca_2Mg_{55}Zn_{43}$. Given that the phases $Ca_xMg_yZn_z$ have almost similar effects on the corrosion behavior of the alloy because of their similarity in the composition and crystallographic parameters [24], all these phases are assumed to be one in the simulation. The computational flow chart based on the aforementioned thermodynamic software is given in Figure 2, which illustrates the predicted phases and their amounts during solidification.

2.1.2. Validation of secondary phase predictions in Mg-Zn-Ca alloy system

In this work, CompuTherm's PANDAT software was used to predict the volume fraction of the final phases based on the alloy compositions. The phases were first determined by X-ray diffraction (XRD) analysis, and the predicted phase volume fractions were then compared with high-resolution Scanning Electron Microscope (SEM) images of actual samples for validation. The phase volume fractions from the SEM micrographs were captured at various magnifications ranging from X200 to X10,000, and their averages were compared with the values predicted by the software. In total, 72 micrographs of the samples were analyzed using this method to determine the average secondary phase fractions. To accurately validate the predictions of secondary phase formation (Mg_2Ca and $Ca_xMg_yZn_z$), the experimental results reported by other researchers were also employed.

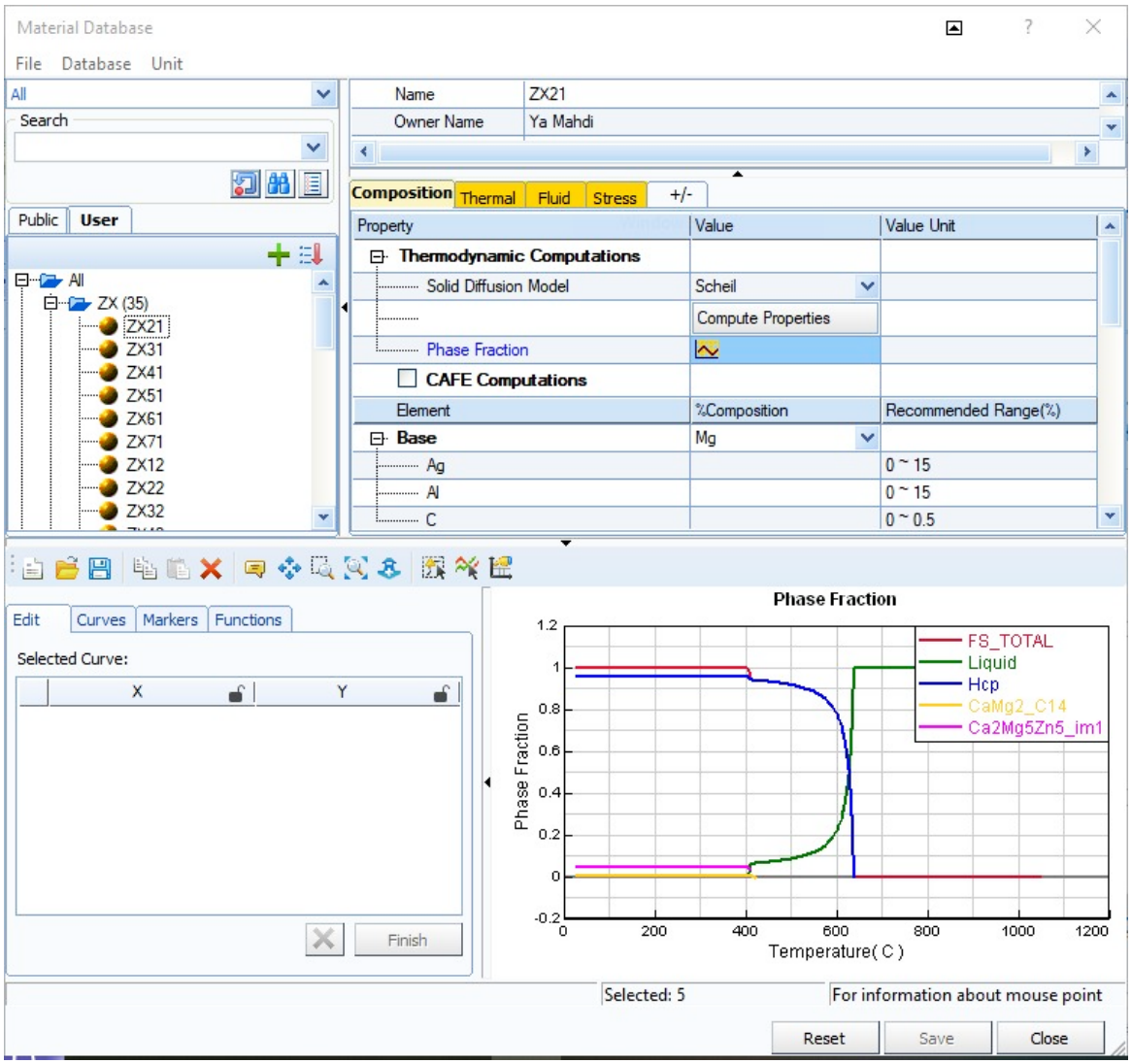

Fig. 1. Representative thermodynamic simulation output generated by CompuTherm's PANDAT software illustrating the predicted phase evolution in an alloy

[DOI: 10.22068/ijmse.4603]

2.1.3. *Prediction of minimum corrosion rate based on secondary phases*

Previous studies on the selected Mg-alloys showed a significant correlation between the type of precipitates and the corrosion rate. Based on the data generated through validated microstructure prediction of the ZX series of Mg-alloys by software, Design-Expert (version 13.0.5.0 2021) software was used along with RSM to determine the optimal alloy composition with the highest corrosion resistance. The weight percentages of the alloying elements served as independent parameters (factors), and the weight percentages of the phases Mg-α, Mg_2Ca, and CaxMgyZnz (obtained from CompuTherm's PANDAT) were treated as dependent parameters (responses). Experimental data from other researchers were incorporated to define optimization criteria aiming at reducing corrosion rates. The following criteria were defined based on the objectives outlined in the introduction:

(1) Minimizing the total of secondary phases, which is equivalent to maximizing the solid solution phase α-Mg.
(2) Minimizing the Mg_2Ca phase, which contributes to micro galvanic corrosion.
(3) Maximizing the $Ca_xMg_yZn_z$ phases, which exhibit relatively lower corrosion rates compared to Mg_2Ca deposits.

Criteria (2) and (3) were implemented in the software to minimize the ratio of $Mg_2Ca/Ca_xMg_yZn_z$.

2.1.4. *Corrosion behavior optimization using statistical model*

To simulate the corrosion resistance of Mg-alloys under study using Design-Expert, the corrosion rate was quantified based on criteria defined through a desirability function. The minimum corrosion rate corresponds to the maximum desirability value at that point.

This function assigns numerical values between 0 to 1 for each composition that the highest value corresponding to the best choice. To validate the statistical model, the predicted alloy composition with minimum corrosion rates based on the volume fraction of secondary phases, a polarization test was adopted. The actual corrosion rate results were compared with the predictions of the desirability function at the points of maximum desirability (minimum corrosion), minimum desirability (maximum corrosion), and middle desirability (average corrosion) to complete the validation process. A summary of the optimization process using Design Expert software is given as follows:

1. **Factors**:
   - Zn: Continuous numeric (1-7 wt%, coded as -1 to +1).
   - Ca: Continuous numeric (1-5 wt%, coded as -1 to +1).
2. **Responses:**
   - R1: Mg(α) volume % (79.12-96.58%).
   - R2: Mg_2Ca volume % (0-9.45%).
   - R3: $Ca_xMg_yZn_z$ volume % (2.31-17.43%).
   - R4: Ratio ($Mg_2Ca/Ca_xMg_yZn_z$, 0-3.873).
3. **Optimization:** Multi-criteria decision making with desirability functions.
4. **Deoptimization:** Reversed criteria to simulate extreme corrosion conditions.
   - Best-Case Solutions: Zn= 2.391 wt%, Ca= 1.000 wt%, Mg(α)= bal.
   - Medium-Case Solutions: Zn= 1.761 wt%, Ca= 4.590 wt%, Mg(α)= bal.
   - Worst-Case Solutions: Zn= 1.000 wt%, Ca= 5.000 wt%, Mg(α)= bal.

The integrated framework combining thermodynamic modeling, (design of experiment) DOE, RSM, and experimental validation for Mg–Zn–Ca alloy design is shown in **Error! Reference source not found.**.

2.2. Materials and Methods

2.2.1. *Sample preparation*

According to simulated results, three alloys representing the lowest, highest and middle desirability were selected for model validation. The alloys were melted in an induction furnace under a protective argon atmosphere to prevent oxidation of the reactive alloying elements. They were subsequently cast into a nickel-free, molybdenum-alloyed steel mold (Mo40), followed by cooling in the mold to room temperature. These selected alloys were analyzed using X-ray fluorescence (XRF) to confirm their chemical compositions, which are detailed in Table 1.

2.2.2. *Corrosion environments*

Two different corrosion environments were used for corrosion behavior evaluations of the selected alloys. The phosphate-buffered saline (PBS) solution was prepared as the electrolyte for bioelectrochemical tests by dissolving PBS salt tablets from Biostar Pharmed in deionized distilled water. For pH change testing, a concentrated 3% (w/w) sodium chloride solution provided by Qatran Chemical Company, with a purity of more than 99%, in deionized distilled water was used. The ionic composition of the solutions used in this study is presented in Table 2.

[DOI: 10.22068/ijmse.4603]

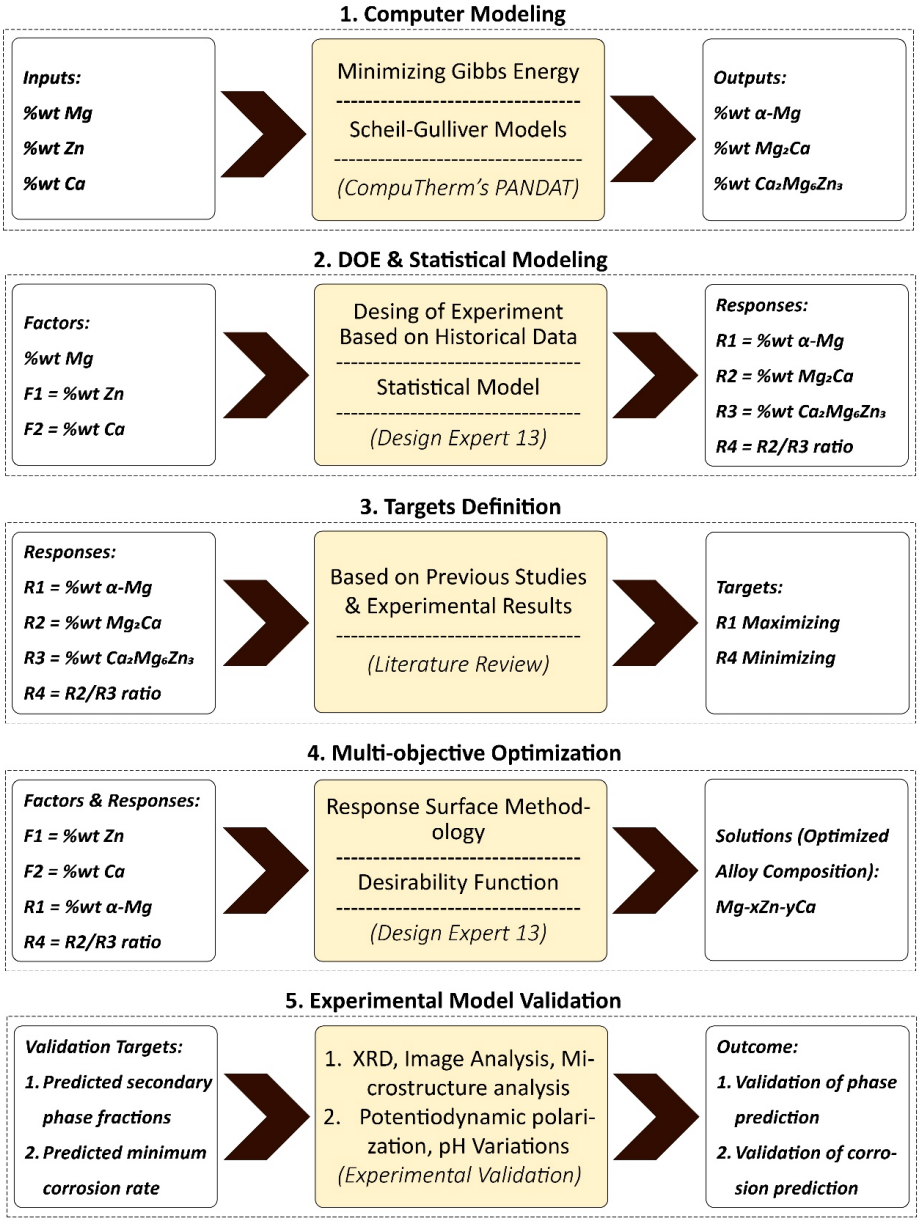

Fig. 2. An integrated framework combining thermodynamic modeling, DOE, RSM, and experimental validation for Mg–Zn–Ca alloy design

Table 1. Chemical composition of different alloy samples

Desirability	Nominal Alloy	Composition %						
		Mg	Zn	Ca	Na	Mn	Fe	Ni
high	ZX31	Bal	2.608	0.968	0.005	0.01	-	-
Medium	ZX24	Bal	2.332	4.036	0.005	0.01	-	-
low	ZX15	Bal	1.349	4.857	0.005	0.01	-	-
Note: The desirability value obtained from the DOE analysis represents the alloy's corrosion resistance.								

Table 2. Nominal ionic concentration of corrosion environment

Environment	Ion Concentration (mM/L)				pH Value
	Na^+	K^+	Cl^-	$HPO_4^{-2}/H_2PO_4^-$	
NaCl	513.3	-	513.3	-	7.24
PBS	137	2.7	139.7	10	7.40

[DOI: 10.22068/ijmse.4603]

2.2.3. *Macroscopic examination*

Macro-level imaging aimed to understand large-scale corrosion mechanisms, including pitting corrosion, or the formation of corrosion products on the metal surface. Samples exposed to pH variation test were captured at different times. The images were taken using a Samsung Electronics digital camera equipped with a macro sensor, with a 5 megapixel resolution and an aperture of F2.4.

2.2.4. *Optical microscopy*

The samples were examined using optical microscopy to assess the microstructure and morphology as well as to validate the volume fraction predictions of phases. The samples were cut to appropriate dimensions and polished manually and mechanically using waterproof SiC abrasive papers with different papers of grit sizes 180 to 5000. For final polishing, a glycerin-ethanol suspension mixed with 0.05 micron diamond abrasive powder was used. The samples were then etched using glycolic acid (Table 3) for 3 to 5 seconds to reveal secondary precipitates. For microstructure analysis, various images at different magnifications were taken using an optical microscope (Huvitz, model HRM-300, South Korea) equipped with a digital camera. Quantitative image analysis of the acquired micrographs to determine the volume fraction of secondary phases was performed using Clemex Vision software (version 3.5, Canada).

Table 3. The etchant composition

Acetic Glycol composition (ml)			
Ethylene Glycol	**Acetic Acid**	**Water**	**HNO_3**
60	20	20	1

2.2.5. *XRD analysis*

Phase identification in the samples was made using XRD for two purposes: validation of the phase prediction by the thermodynamic simulation software and confirmation of the presence of secondary phases affecting the corrosion behavior in the microstructure. The XRD analysis was performed using a D8 ADVANCE diffractometer from Bruker, Germany. Measurements were carried out with a copper anode (Cu-Kα, λ= 1.5406 Å) in the diffraction angle range 2θ (5-85°) at 25°C. The resulting diffraction patterns were analyzed using HighScore Plus software (version 3.0e 2012), employing the COD database (2013-2024) along with related literature for phase identification.

2.2.6. *Bioelectrochemical test*

Bioelectrochemical experiments were conducted using the potentiodynamic polarization method with a PalmSens3 potentiostat/galvanostat. Three selected samples were tested using an Ag/AgCl reference electrode and a counter electrode in PBS electrolyte solution. The surfaces of all samples were prepared by SiC abrasive papers with mesh sizes ranging from 200 to 5000 and then mirror-polished using diamond particles (0.05 μm) suspended in an ethanol-glycerin mixture. After polishing, the samples were degreased and cleaned with ethanol, acetone, and dry air spray (dust cleaner). A linear sweep technique with a voltage range of -1 to -3 V and a scanning rate of 5 mV/s was used to record the current polarization curves as a function of voltage. The area of the sample in contact with the electrolyte was measured with a caliper with an accuracy of (±0.01 mm), and the current density (i) was calculated by dividing the measured current by the contact area, in μA/cm².

2.2.7. *pH variation test*

The pH variation test is an indirect method for investigating the corrosion rate and mechanism in the long term. The samples were prepared in the same manner as the bioelectrochemical test, and a 3% NaCl solution was used as the corrosion medium for 8 days. The pH changes over time were measured using a NetPil pen pH-meter with an accuracy of 0.01.

3. RESULTS AND DISCUSSION

3.1. Validation of Phase Volume Fraction Predictions

The volume fraction prediction of the formed phases during casting solidification of alloys was performed using CompuTherm software. To effectively use these results, it is necessary to identify the phases and compare the actual and predicted volume fractions of the formed phases.

The phase diagram of the ternary Mg-Zn-Ca alloy system (Figure 3) shows that, upon cooling of Mg-rich alloys, secondary phases such as Mg_2Ca and $Ca_2Mg_6Zn_3$ may form, ultimately leading to a ternary eutectic transformation (Equation 1). Figure 3 was adapted and modified from Ref. [38]. When the Ca content relative to Zn is low (wt% Ca/Zn$\leq \frac{1}{11}$), the Mg_2Ca phase is not formed, and all the Ca precipitates in the form of the $Ca_2Mg_6Zn_3$ phase. In this case, the intermediate MgZn phase crystallizes first and completely solidifies during the ternary eutectic transformation, as shown below [38]:

$$L \rightarrow \alpha\text{-}Mg + Ca_2Mg_6Zn_3 + Mg_2Ca \quad (1)$$

$$L \rightarrow \alpha\text{-}Mg + Mg_{12}Zn_{13} + Ca_2Mg_6Zn_3 \quad (2)$$

[DOI: 10.22068/ijmse.4603]

At the chemical composition point of approximately wt% Ca/Zn≈ 1/4, solidification of the alloy occurs homogeneously, and the entire melt completely solidifies in a layered eutectic transformation as given in Equation 3:

$$L \rightarrow \alpha\text{-}Mg + Ca_2Mg_6Zn_3 \quad (3)$$

Based on the ternary equilibrium diagram, it is predicted that during equilibrium solidification, the final phase structure of the ZX31 alloy will contain $Ca_2Mg_6Zn_3$ precipitates, and the two others will also contain Mg_2Ca.

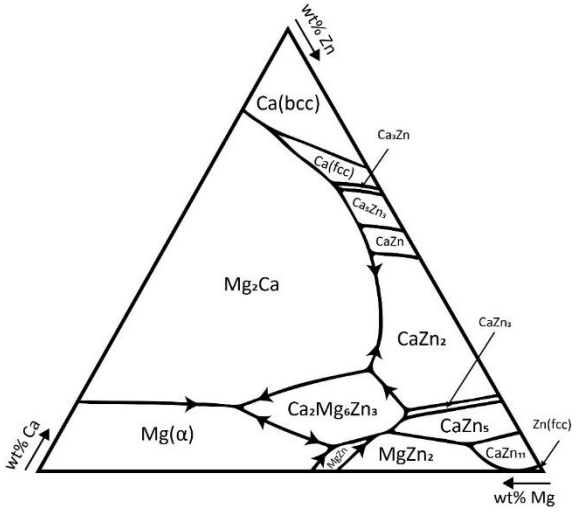

Fig. 3. Ternary phase diagram of Mg-Zn-Ca alloy system

3.1.1. Qualitative validation based on XRD results

Qualitative validation of the volume fraction of the predicted phases was performed using XRD analysis. The XRD analysis allows for the qualitative identification of phases. The results of the phase analysis are shown in Figure 4. The results show that the expected phases are formed in all three samples. In the case of sample ZX31, the presence of the Mg_2Ca phase is due to quasi-equilibrium solidification conditions; however, in the XRD analysis, the low intensity of the Mg_2Ca peaks indicates the presence of a small amount of this phase, which is meaningful given the dilute Ca content of the ZX31 composition and the limited thermodynamic driving force for its formation under non-equilibrium conditions. It is important to note that the general agreement between the XRD-identified phases and the CompuTherm's PANDAT predictions validates the reliability of the thermodynamic database (PanMg) employed in this study for the Mg-Zn-Ca ternary system.

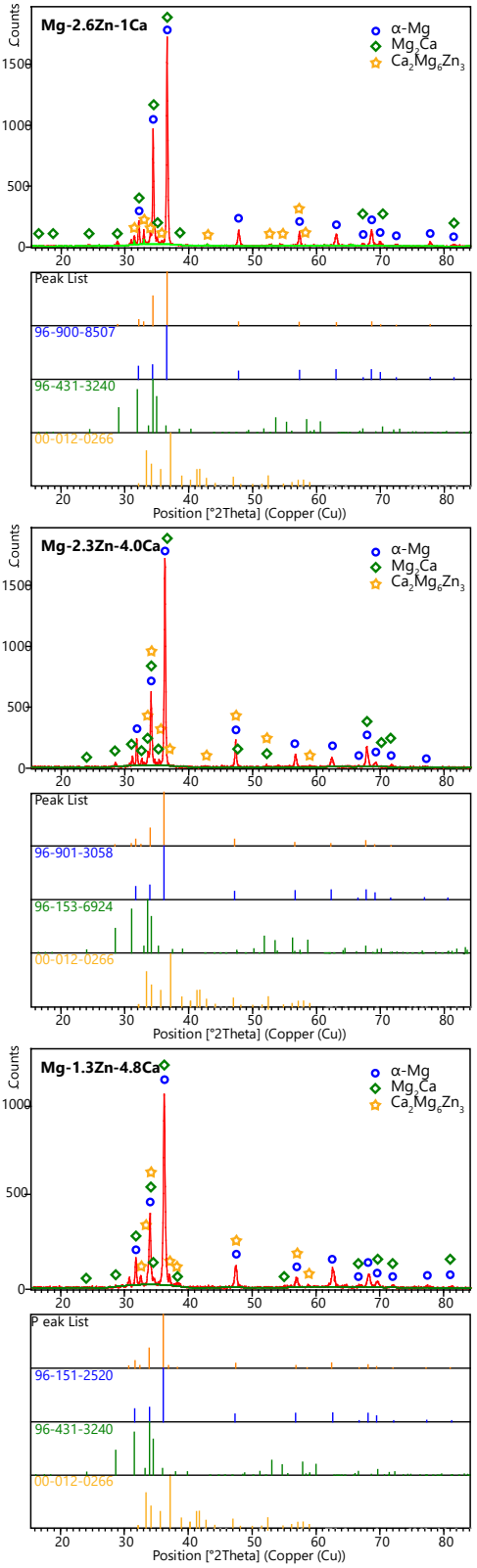

Fig. 4. XRD patterns of samples with varying compositions. The diffraction peaks are indexed according to standard reference cards, confirming the presence and relative amounts of the primary α-Mg matrix phase along with precipitates including $Ca_2Mg_6Zn_3$ and Mg_2Ca phases

[DOI: 10.22068/ijmse.4603]

The minor discrepancy observed in sample ZX31 does not undermine the overall predictive capability of the model; rather, it highlights the sensitivity of phase evolution to solidification kinetics, alongside thermodynamic parameters. It is important to emphasize that, in the present study, XRD analysis was employed exclusively for the qualitative identification of the phases present in the microstructure. Quantitative determination of secondary phase volume fractions was instead obtained independently through systematic image analysis of micrographs, as described in the following section.

3.1.2. Quantitative validation based on microscopic images

To complement the qualitative XRD validation, a quantitative assessment of the predicted phase volume fractions was conducted through systematic microstructural image analysis. Since the densities of the phases formed are relatively similar, the weight fractions of the phases (as predicted by the software) were assumed to be approximately equivalent to their volume fraction, thereby enabling a direct and meaningful comparison between computational predictions and experimental measurements.

Based on the respective crystal structure parameters, the theoretical densities of the α-Mg matrix (P63/mmc, hP2 [39]), the $Ca_2Mg_6Zn_3$ phase ($P\bar{3}1c$ [40], hP22 [39]), and the Mg_2Ca phase (P63/mmc, hP12 [41]) were calculated to be approximately 1.74–1.77 [42-44], 1.72, and 1.72 [41] g/cm³, respectively. The proximity of these theoretical densities confirms that these phases of the Mg-Zn-Ca system possess similar mass densities, thereby supporting the accuracy of equating weight and volume fractions for the present image-analysis-based validation. This approach was also adopted in previous studies, as reported by Schäublin et al. [45]. The steps of analyzing the selected images are detailed in Figure 5.

It is noted that image analysis has also been used by other researchers to evaluate the weight fraction of phases appeared in the alloy microstructure. Doležal et al. [46] investigated the microstructure and mechanical properties of Mg-3Zn-2Ca bioalloy under different manufacturing conditions, demonstrating that image analysis provides reliable estimates of secondary phase fractions consistent with other characterization techniques. Ibrahim [47] used this method to study the properties of Mg-xZn-0.5Ca alloys (x= 1.2, 1.4, and 1.6 wt%), establishing a correlation between phase distribution and mechanical performance relevant to bone fixation device applications. Cha et al. [48] provided high-resolution SEM images of Mg-xZn-5Ca alloys (x= 0.5, 1.1, and 3 wt%), which were incorporated into the present analysis to expand the validation dataset in a broader composition range. The convergence of results from these independent studies strengthens the reliability of image analysis as a quantification method in the present work. The comparison between the predicted values by the software and the experimental results is presented in Figure 6.

A particular challenge encountered in the analysis of dilute alloy compositions is the difficulty in accurately measuring secondary phases due to their low volume fraction and the microstructural inhomogeneities inherent to as-cast samples. Additionally, artefacts introduced during sample preparation, such as mechanical deformation of the soft Mg matrix or phase pull-out during polishing, can obscure phase boundaries and reduce measurement accuracy. To overcome these limitations, high-resolution SEM images sourced from previous studies ([20, 46, 49–54]) were employed, in which phase identification had been confirmed through energy dispersive X-ray spectroscopy (EDS) point analysis before image analysis. The comparison of the predicted values versus the experimentally measured results in the images is illustrated in Figure 7.

The degree of agreement between CompuTherm's PANDAT predictions and the experimentally measured phase fractions was statistically evaluated using the **Pearson's correlation coefficient (R)**, which quantifies the linear relationship between the two datasets. The *p*-value was also examined to determine the meaningfulness of the outcomes, such that *p*-values less than 0.05 were considered significant correlations. The results are shown in Table 4, which indicate a statistically significant correlation between the predicted and actual values. The strong correlation coefficient confirms that the CompuTherm's PANDAT thermodynamic model accurately captures the phase formation behavior in the Mg-Zn-Ca alloy system and can therefore be reliably employed as a predictive design tool for optimizing alloy compositions without the need for exhaustive trial-and-error experimentation. Collectively, the qualitative XRD validation and quantitative image analysis results establish a robust experimental foundation that supports the predictive accuracy of the simulations. These findings demonstrate that CompuTherm's PANDAT-based phase prediction, when validated against experimental

[DOI: 10.22068/ijmse.4603]

data, constitutes an effective and efficient strategy for guiding the compositional design of biodegradable Mg-Zn-Ca alloys with tailored phase constitutions and, consequently, optimized corrosion performance.

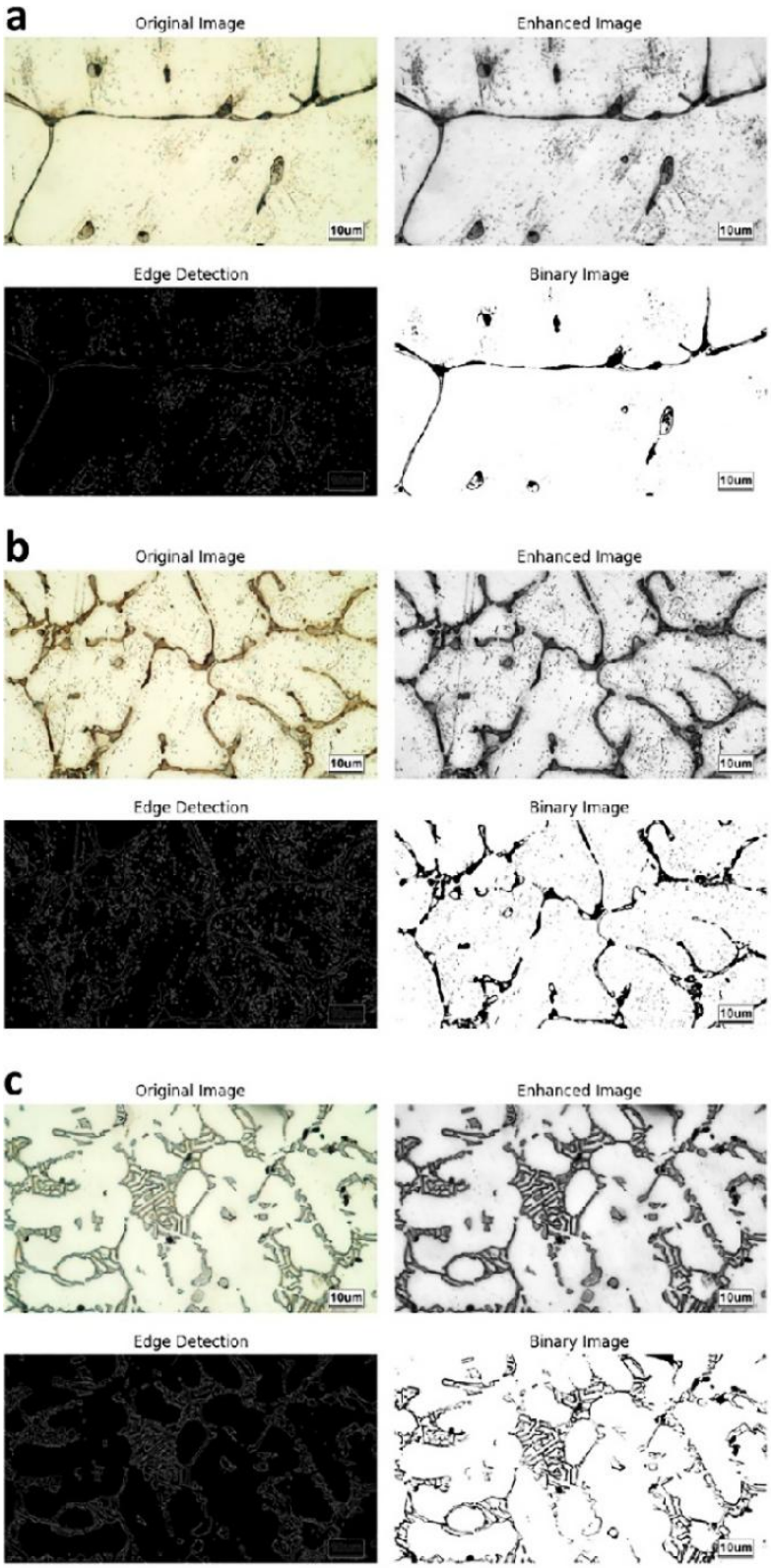

Fig. 5. Steps for analyzing metallographic images from the samples, a) ZX31, b) ZX24, and c) ZX15, including original images, enhanced image, edge definition, and binary image

[DOI: 10.22068/ijmse.4603]

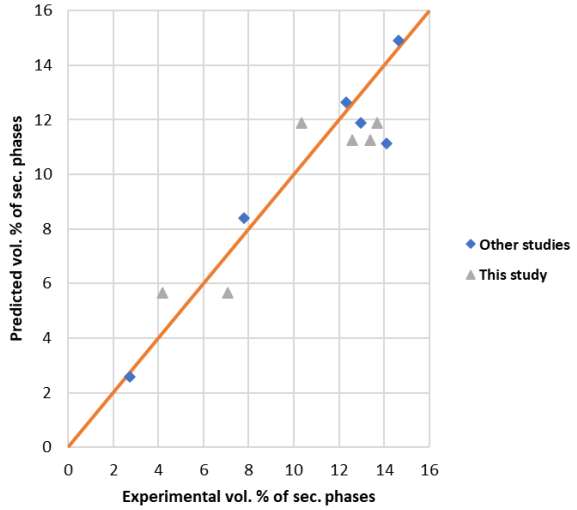

Fig. 6. Comparison between the total values of secondary phases predicted by CompuTherm software vs. values obtained from the image analysis of actual samples from the present study and other studies [46-48]

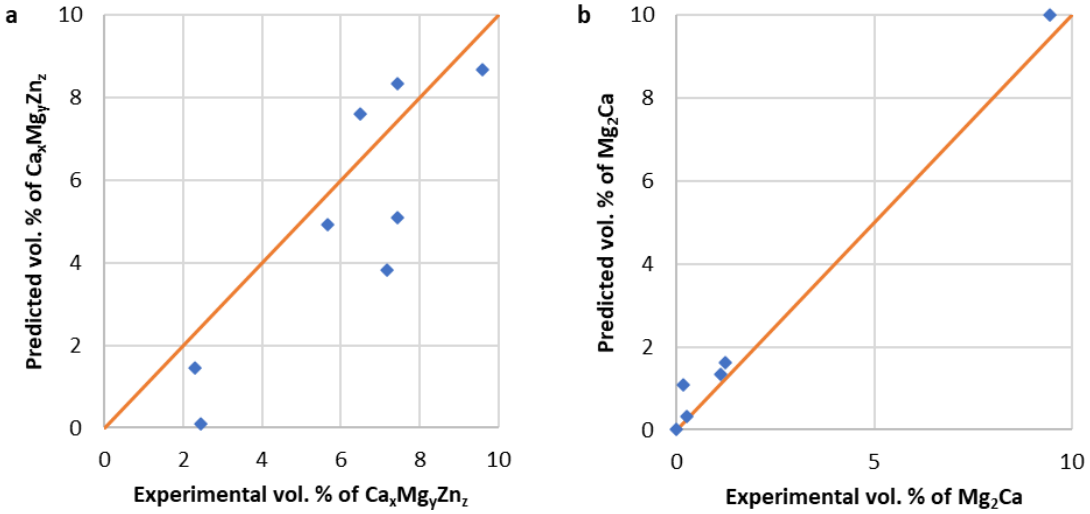

Fig. 7. Comparison between the secondary phase values a) $Ca_xMg_yZn_z$ and b) Mg_2Ca predicted by CompuTherm software vs. values obtained from image analysis of samples reported in previous studies [20, 46, 49–54]

Table 4. Pearson coefficient, p-value, and significance of phase prediction by CompuTherm software

Item (vol%)	Number of Samples (n)	Pearson's Correlation Coefficient (R)	*p*-Value	Meaningfulness (alpha= 0.05)
Total secondary phases	12	0.9368	< 0.001	Significant
$Ca_xMg_yZn_z$	8	0.8696	0.005	Significant
Mg_2Ca	6	0.9961	< 0.001	Significant

3.2. Microstructure Analysis

The optical microscope images of the ZX31 alloy are presented in Figure 8. As shown in Figure 8, the secondary precipitates in the ZX31 alloy have two dominant morphologies: dendritic and spherical. Dendritic precipitates form island-like structures, predominantly along grain boundaries, while spherical precipitates nucleate and grow preferentially within the grain interiors. This spatial distribution is thermodynamically governed by the solidification sequence; grain boundary regions, being the last to solidify, are enriched in solute elements (Zn and Ca) due to microsegregation, thereby providing a chemically favourable environment for the nucleation of $Ca_2Mg_6Zn_3$ intermetallic compounds in a dendritic morphology. In contrast, the intragranular spherical precipitates are believed to form during solid-state

[DOI: 10.22068/ijmse.4603]

cooling following primary α-Mg solidification, where the reduced driving force for growth favours isotropic, low-energy spherical morphology over anisotropic dendritic growth [40, 55]. Dendritic and spherical precipitates have a eutectic structure (α-Mg + $Ca_2Mg_6Zn_3$), as indicated by the red arrows in Figure 8-d. As shown in Figure 9, a larger volume of secondary precipitates is formed in the ZX24 alloy, which is due to the increased Ca content in the alloy. These precipitates are characterized by a dendritic morphology with greater thickness and continuity around the dendrites. In this alloy, intragranular spherical phases are rarely observed, and fine, spot-like precipitates are formed around the dendritic phases and near the tips of the dendrites, as shown by the red arrows in Figure 9-d. With further increase in Ca in sample ZX15, a predominantly dendritic microstructure appears, in which precipitates with a pattern resembling a Chinese script-like pattern (Figure 10) are formed in the spaces between the dendrites. Due to the position of the alloy in the Mg-Zn-Ca ternary phase diagram, a significant amount of Mg_2Ca precipitates from the molten phase and finally solidifies at the α-Mg + $Ca_2Mg_6Zn_3$ + Mg_2Ca eutectic point. Collectively, the progressive microstructural evolution from ZX31 to ZX15, characterised by the transition from sparse spherical precipitates to a continuous dendritic network and ultimately to a Chinese script eutectic structure, reflects the systematic shift in solidification pathway driven by increasing Ca content. These observations are in excellent agreement with the thermodynamic phase predictions in the investigated alloys.

3.3. Corrosion Behavior Analysis

3.3.1. Potentiodynamic polarization tests

The results of the potentiodynamic polarization tests in PBS for different samples are shown in Figure 11. The overall reaction of Mg in an aqueous environment that results in a hydroxide layer alongside hydrogen gas evolution is given by Equation 4.

$$Mg_{(s)} + 2H_2O_{(l)} \rightarrow Mg(OH)_{2(s)} + H_{2(g)} \quad (4)$$

Equations 5 and 6 can represent the reactions between Mg and the $Mg(OH)_2$ layer with ions dissolved in Cl-containing environments [13]. The aggressive Cl^- ions present in PBS disrupt the continuity of the hydroxide layer through the two mentioned competing reactions, in which both the metallic Mg substrate and the $Mg(OH)_2$ layer react with Cl^- to form highly soluble $MgCl_2$:

$$Mg_{(s)} + 2Cl^-_{(aq)} \rightarrow MgCl_2 + 2e^- \quad (5)$$

$$Mg(OH)_{2(s)} + 2Cl^-_{(aq)} \rightarrow MgCl_2 + 2OH^- \quad (6)$$

The conversion of the $Mg(OH)_2$ to soluble $MgCl_2$ is particularly detrimental, as it effectively removes the protective hydroxide layer from the alloy surface, continuously exposing Mg to the corrosive electrolyte. This mechanism explains the characteristically high and sustained corrosion rates observed for Mg alloys in Cl-rich physiological media compared to simpler aqueous environments [56].

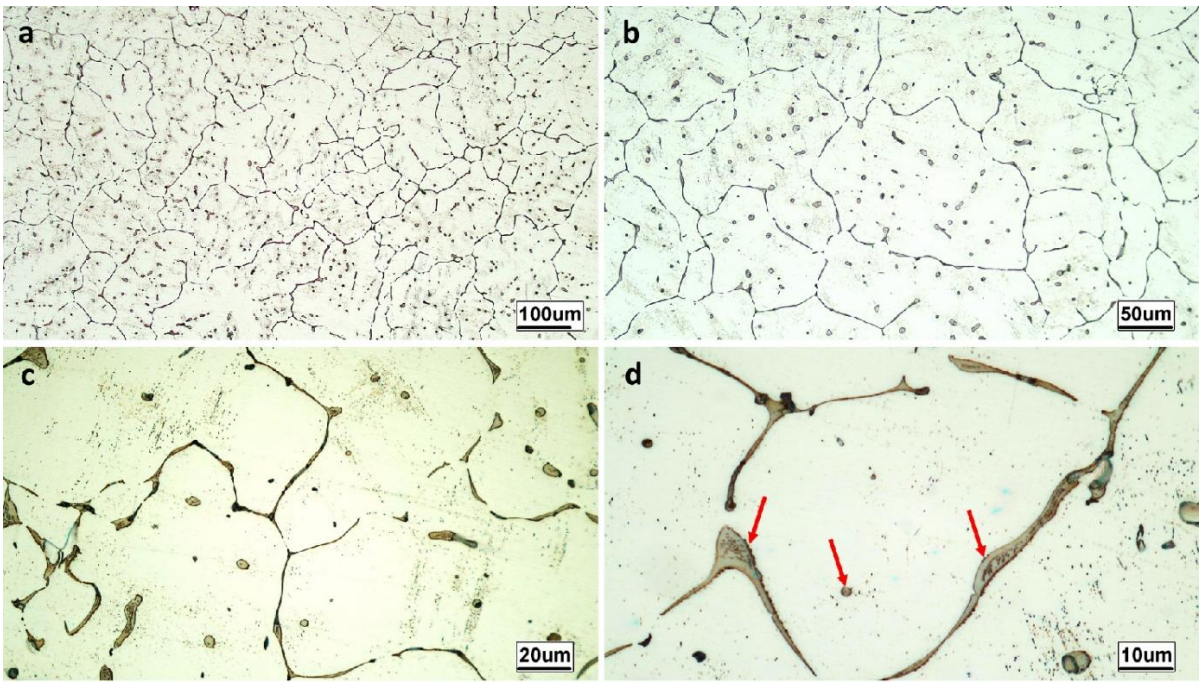

Fig. 8. Optical micrograph of as-cast ZX31 (the best)

[DOI: 10.22068/ijmse.4603]

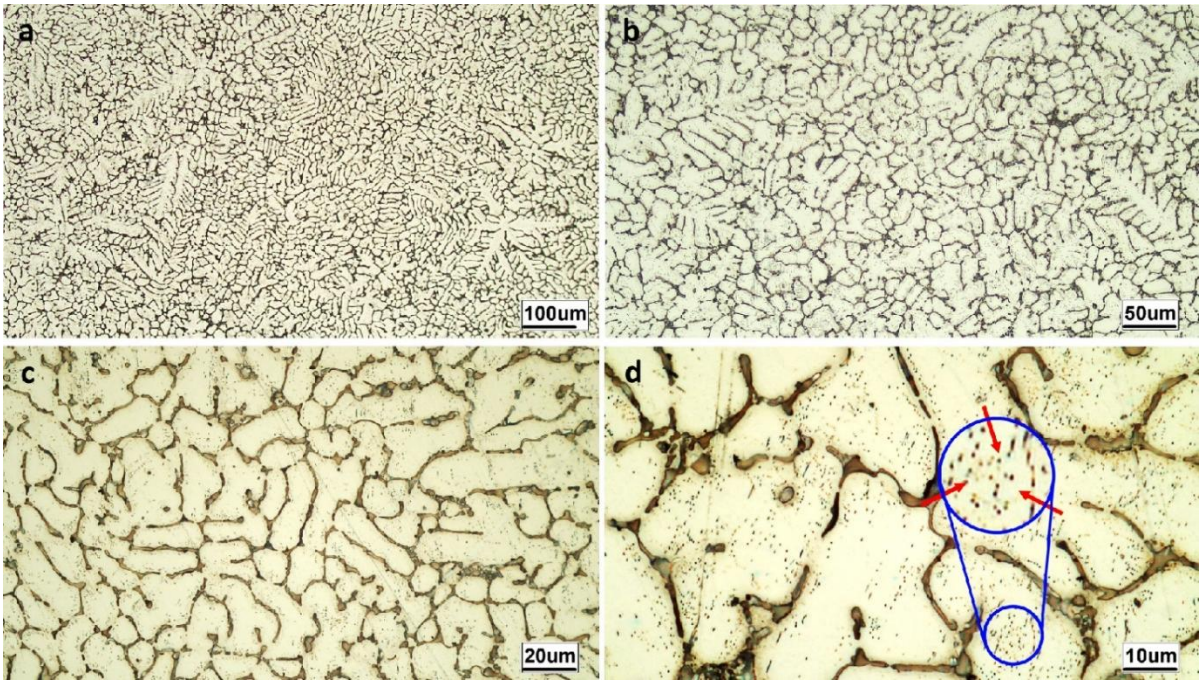

Fig. 9. Optical micrograph of as-cast ZX24

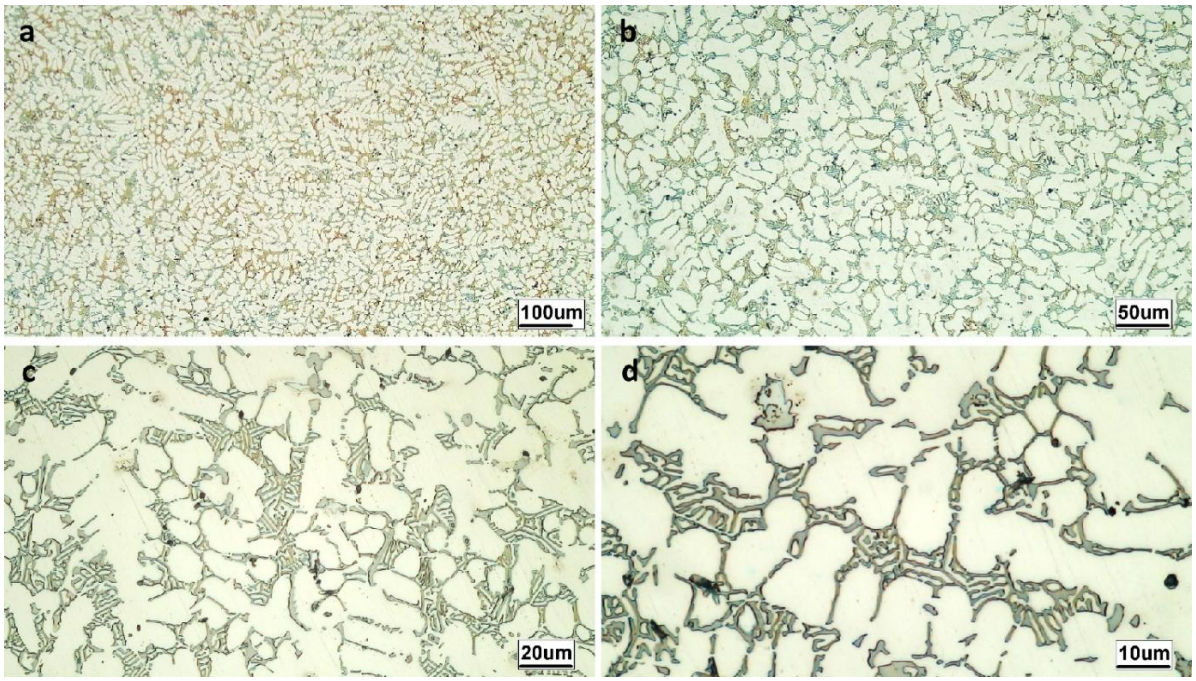

Fig. 10. Optical micrograph of as-cast ZX15 (the worst)

Polarization curves show the anodic and cathodic behaviors of the three alloys with different microstructures. The corrosion potential (E_{corr}) is a thermodynamic indicator that indicates the intrinsic tendency to corrosion (more negative values mean more tendency to corrosion), while the corrosion current (I_{corr}) indicates the corrosion kinetics [20, 57]. The polarization curves show that ZX31 alloy exhibits the most positive E_{corr} and the lowest I_{corr}. As the Ca content in the alloys increases, the E_{corr} values become more negative, indicating an increase in electrochemical activity. The decrease in Zn also exacerbates this trend. According to the electrochemical series (Table 5), the electrochemical potentials for the reduction of Zn^{2+}, Mg^{2+}, and Ca^{2+} move towards more negative values (indicating

[DOI: 10.22068/ijmse.4603]

greater activity) with increasing Ca content [58]. With increasing Ca content or decreasing Zn content in ZX31, ZX24 and ZX15 alloys, the electrochemical potential decreases (more negative values or increased corrosion tendency), which aligns with the theoretical fundamentals. The parameter I_{corr} increases with increasing Ca content and decreasing Zn content in the alloys, indicating an increase in corrosion rate. It can be rationalised in terms of the micro-galvanic coupling between the $Ca_2Mg_6Zn_3$ and Mg_2Ca intermetallic phases and the surrounding α-Mg matrix. The values of I_{corr} and other corrosion parameters, including E_{corr}, anodic (β_{anodic}), and cathodic ($\beta_{cathodic}$) polarization slopes, were extracted by Tafel Extrapolation add-in of OriginPro software (version 10.1.0.178 2024) and are tabulated in Table 6. The relationship between I_{corr} (in mA/cm²) and the average corrosion rate (CR_i in mm/year) (Equation 7) can be used to compare the relative corrosion rates of the alloys [59–61].

$$CR_i = 22.854\ I_{corr} \quad (7)$$

The corrosion rate values derived from Equation 7 confirm the trend established by the electrochemical parameters and are in good agreement with the findings reported by Cha et al. [48] and Zander and Zumdick [62] for Mg-Zn-Ca alloys with comparable compositions, lending further confidence to the validity of the present electrochemical measurements.

3.3.2. The pH variations

The results of the pH variation test in the NaCl solution are shown in Figure 12. This test evaluates the long-term corrosion behavior of the material, unlike short-term electrochemical tests. The initial pH of the solution for all three samples was 7.24, which gradually increased with time. The increase in pH level in the saline solution indicates that more hydroxide ions (OH^-) are produced as Equation 6 progresses. Additionally, the compound $Mg(OH)_2(s)$ is produced from the overall corrosion reaction of Mg in aqueous media according to Equation 4. As demonstrated in Figure 12-a, significant pH fluctuations occur in the early stages, indicating a dynamic and spatially heterogeneous corrosion process on the alloy surface, rather than uniform dissolution.

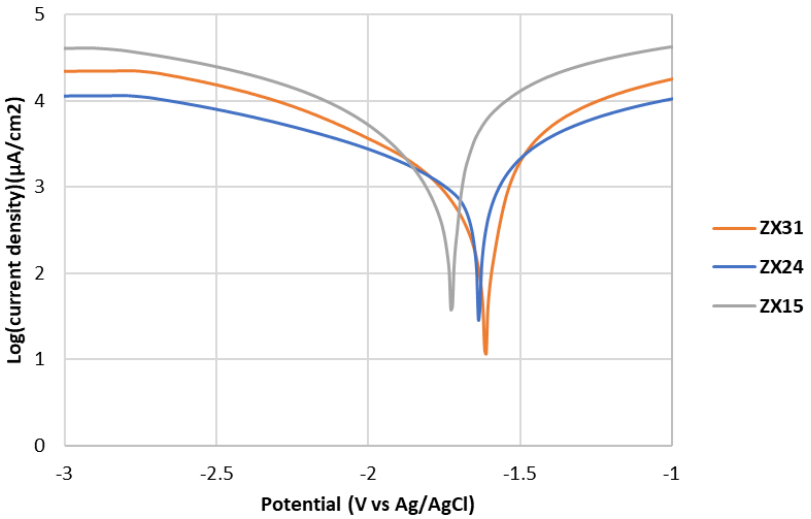

Fig. 11. Anodic-cathode curve of the potentiodynamic polarization test in PBS electrolyte for the three alloys

Table 5. Position of some elements in the electrochemical potential series

Element	Half-reaction			E° (V vs SHE)
Ca	$Ca^{2+} + 2e^-$	⇌	Ca(s)	-2.868
Mg	$Mg^{2+} + 2e^-$	⇌	Mg(s)	-2.372
Zn	$Zn^{2+} + 2e^-$	⇌	Zn(s)	-0.7618

Table 6. Corrosion parameters obtained from polarization corrosion tests for selected alloys

Sample	E_{corr} ($V_{Ag/AgCl}$)	I_{corr} (μA/cm²)	β_{anodic} (V/decade)	$\beta_{cathodic}$ (V/decade)	CR_i (mm/year)
ZX31	-1.6336	216	0.14	-0.18	4.94
ZX24	-1.6375	514	0.22	-0.37	11.75
ZX15	-1.7753	670	0.17	-0.19	15.33

[DOI: 10.22068/ijmse.4603]

Mechanistically, this behavior is consistent with the initiation and propagation of pitting corrosion, as illustrated in Figure 13. The localised acidification within the developing pits, caused by hydrolysis of dissolved Mg^{2+} ions, temporarily counteracts the alkalinisation of the solution, resulting in the oscillatory pH observed in the early stages. After 24 hours, the rate of pH shows a slower increase (Figure 12-b), indicating a slowdown in the corrosion reaction due to the deposition of salts on the sample surfaces, especially in ZX31 and ZX24. The formation of this surface barrier layer reduces the effective surface available for electrochemical reactions, thereby weakening both the anodic dissolution of Mg and the associated OH^- production. The relatively earlier stabilisation of pH observed in ZX31 compared to ZX24 and ZX15 suggests that the corrosion product layer formed on the lower-Ca alloy is more compact and adherent, providing more effective surface coverage. The varying corrosion rates over time highlight the importance of long-term corrosion testing alongside short-term tests for better understanding the corrosion mechanisms.

3.4. Validation of Corrosion Rate Optimization

The alloy compositions with the highest and lowest corrosion resistance predicted by the statistical optimization software are summarised in Table 7. The corrosion rates derived from potentiodynamic polarization measurements (Equation 7) were determined to be 4.94 mm/y for ZX31, 11.75 mm/y for ZX24, and 15.33 mm/y for ZX15, demonstrating a systematic increase in corrosion rate with increasing Ca content and decreasing Zn content across the alloy series. These experimentally measured values are in close agreement with the rankings predicted by the statistical model (see Table 6), thereby validating the predictive capability of the optimization framework for the Mg-Zn-Ca alloy system. Although the coarseness of the secondary phase precipitates in ZX31 alloy can be a factor in increasing the corrosion rate, a noteworthy observation is that this alloy exhibits the lowest corrosion rate compared to ZX24 and ZX15. Intuitively, coarser precipitates would be expected to intensify micro-galvanic corrosion by increasing the cathode-anode interfacial area; however, in the present case, the larger precipitate size in ZX31 does not lead to a higher corrosion rate. This evidence suggests that the volume fraction of the secondary phase and its type may be the dominant factors in the corrosion rate compared to other factors such as the size of precipitates.

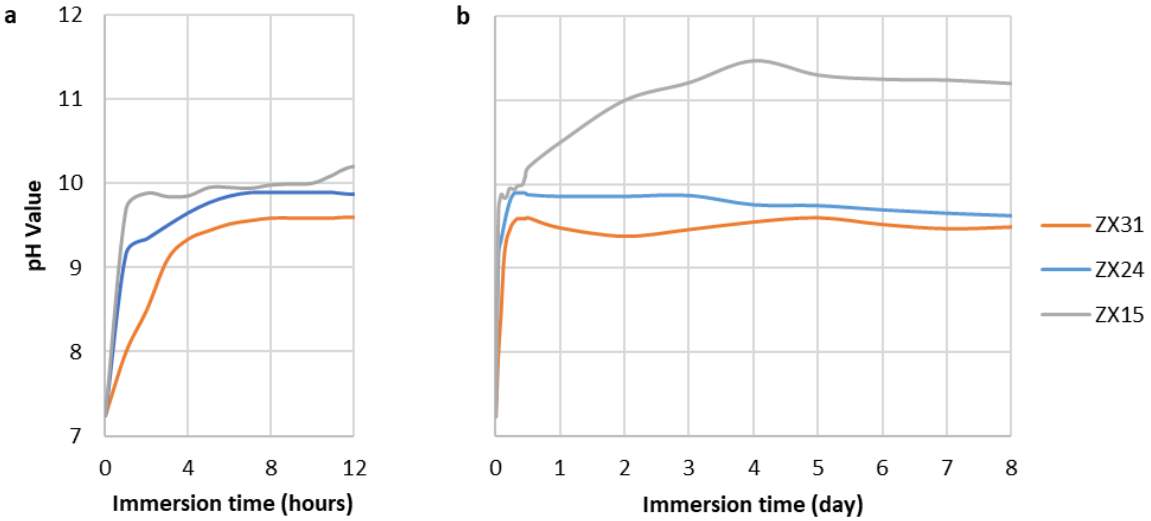

Fig. 12. Graph of changes in pH values over time; a) hours, b) days of immersion

Table 7. The outputs from statistical modeling of software predictions: best, worst, and medium corrosion resistant

Sample	Nominal Composition		Predicted Vol% of Phases and Ratio				Desirability index	Experiment label
	Zn	Ca	Mg (α)	Mg_2Ca	$Ca_xMg_yZn_x$	Ratio (Mg_2Ca/ $Ca_xMg_yZn_z$)		
Best	2.391	1.000	94.875	0.133	4.994	0.000	0.950	ZX31
Medium	1.960	4.432	87.850	7.264	4.887	1.936	1.000	ZX24
Worst	1.000	5.000	88.133	9.534	2.334	3.201	0.632	ZX15

[DOI: 10.22068/ijmse.4603]

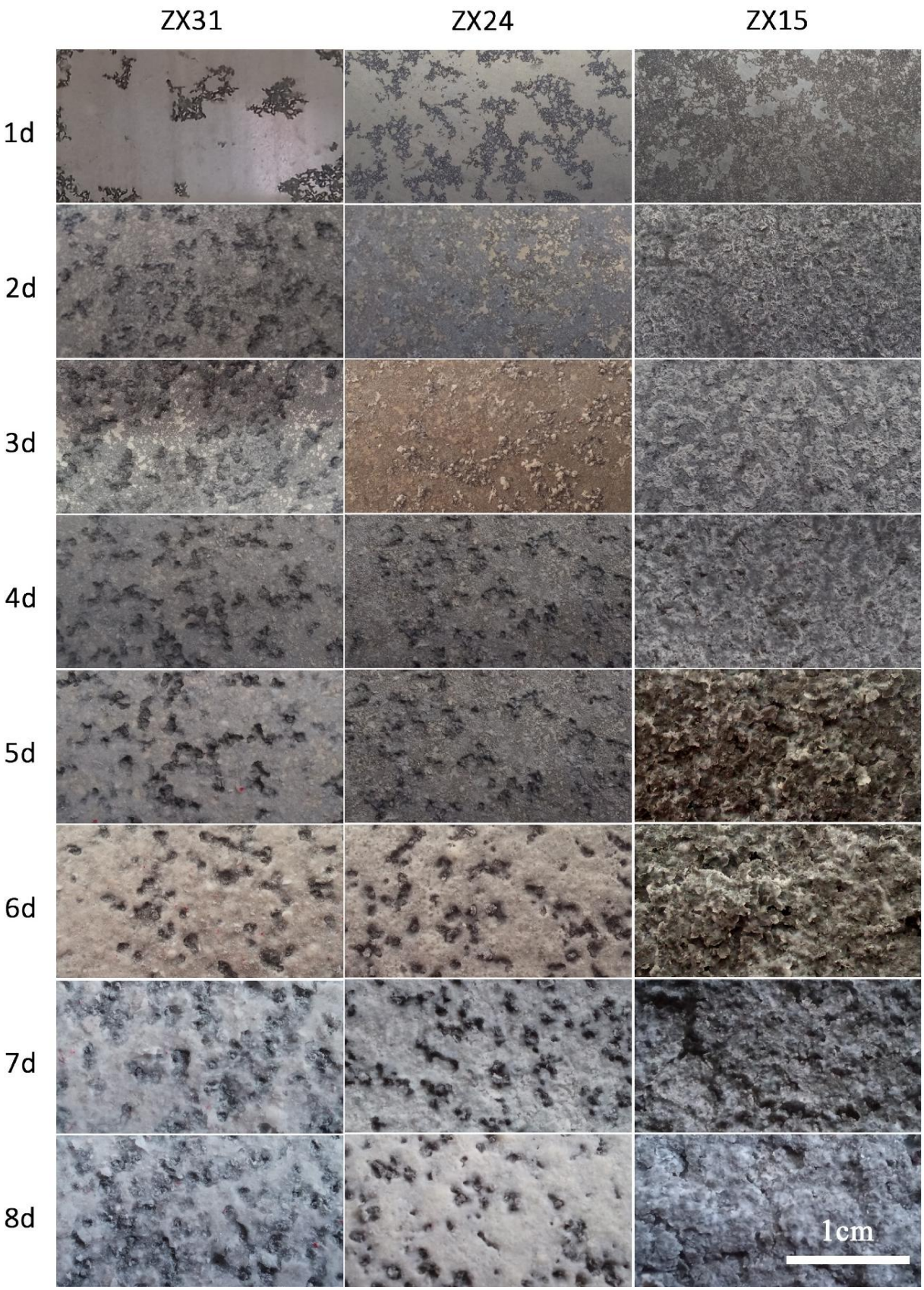

Fig. 13. Macroscopic images of the corrosion surface of samples immersed in 3% NaCl solution

[DOI: 10.22068/ijmse.4603]

The present findings are consistent with those reported by Lu et al. [63]. Moreover, the isolated and discontinuous distribution of precipitates in ZX31, as established in the microstructural analysis, prevents the penetration of corrosive electrolyte and leads to more localized corrosion [64]. After validating the statistical optimization method, the gradient in Figure 14 was plotted based on the desirability index. The desirability index is a dimensionless metric ranging from 0 to 1 that quantifies the degree to which a given alloy composition simultaneously satisfies all defined criteria [65]. The gradient map shows that the red areas have higher corrosion resistance, while the blue areas have lower corrosion resistance. These findings are consistent with the research of Hagihara et. al [66], who also identified the type of secondary phases as a key factor affecting the corrosion rate in this series of alloys. The desirability gradient map of Figure 14 extends the utility of this framework beyond the three alloys experimentally investigated, enabling the prediction of corrosion performance over a continuous range of alloy compositions. Compared to conventional trial-and-error approaches, the present framework substantially reduces the number of experimental iterations required to identify optimal alloy compositions in the development of next-generation biodegradable orthopaedic implants. The strong agreement between the experimentally measured corrosion rates, the thermodynamic phase predictions from CompuTherm's PANDAT software, and the statistical optimization demonstrates the effectiveness of the optimization framework used in this study.

4. CONCLUSIONS

An integrated optimization framework was used to perform thermodynamic and statistical simulations and design a Mg-biodegradable alloy in the Mg-Zn-Ca alloy system with optimum corrosion resistance. First, the microstructure evolution of alloys was predicted using CompuTherm's PANDAT software, and then the predicted microstructure was employed to optimize the corrosion behavior using RSM. The validation of thermodynamic simulated results confirmed the high accuracy of CompuTherm predictions for precipitating phases in the Mg-Zn-Ca alloy system. Both XRD and microstructural analyses showed strong compliance of the formed $Ca_2Mg_6Zn_3$ and Mg_2Ca phases with the predicted values. Statistical image analysis revealed a significant correlation ($R > 0.9368$, $p < 0.001$) between the predicted and experimental values of total secondary phases, confirming that the software is able to reliably predict forming phases.

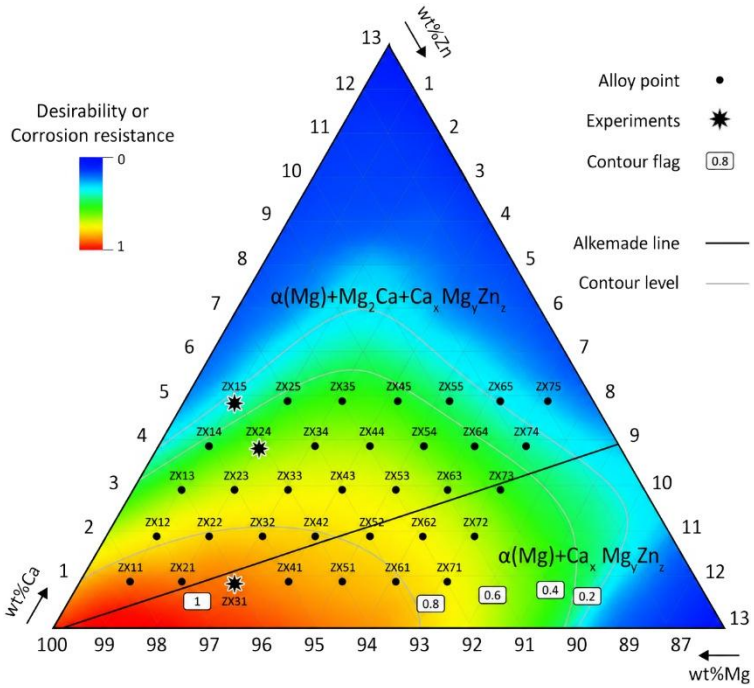

Fig. 14. Ternary phase diagram of Mg-Zn-Ca in the studied section and the gradient of corrosion resistance tendency. Note: Completely blue regions indicate compositions outside the scope of the present investigation and have not been evaluated; their appearance holds no physical interpretation within the framework of this study

[DOI: 10.22068/ijmse.4603]

Microstructural analysis shows that increasing Ca content significantly affects the volume fraction and morphology of secondary phases. The precipitates of ZX31 alloy show mixed dendritic and spherical morphology, while higher Ca in ZX24 alloy promotes the formation of thicker and continuous dendritic phases with minimal intragranular spherical precipitates. At the highest Ca content (ZX15), the matrix morphology is predominantly dendritic, with Chinese script-like precipitates. The results confirm that Ca addition promotes the formation of $Ca_2Mg_6Zn_3$ and Mg_2Ca in ZX alloys.

The decreasing Zn/Ca ratio decreases E_{corr} and increases I_{corr}, indicating faster corrosion. Among the studied alloys, ZX31 exhibits the highest corrosion resistance with the most positive E_{corr}, while ZX15 exhibits the highest activity in electrochemical tests. The results of the pH variation test show that all ZX alloys gradually increase the pH of the solution. These changes have fluctuations in the early stages due to localized corrosion, but the overall trend of the long-term test is similar to the short-term condition. Corrosion rates of ZX31, ZX24, and ZX15 calculated based on the I_{corr} were found to be 4.94, 11.75, and 15.33 mm/y, respectively. The ranking of ZX31, ZX24, and ZX15 as the best to worst alloys is consistent with the predicted results based on the volume fraction of the phases. Overall, this validated framework provides a reliable method to optimize Mg-based biomaterials.

DATA AND CODE AVAILABILITY

The data that support the findings of this study are available from the corresponding author upon reasonable request.

FUNDING STATEMENT

This research received no external funding.

CONFLICT OF INTEREST STATEMENT

The authors declare that they have no conflict of interest.

REFERENCES

[1] X. Huang, X. Liu, Y. Shang, F. Qiao, G. Chen, Current Trends in Research on Bone Regeneration: A Bibliometric Analysis, Biomed Res. Int. 2020 (2020) 1–12. https://doi.org/10.1155/2020/8787394.

[2] L.G. Griffith, G. Naughton, Tissue engineering-current challenges and expanding opportunities., Science 295 (2002) 1009–1014. https://doi.org/10.1126/science.1069210.

[3] M. Dash, Biomimetic Biomaterials for Tissue Regeneration and Drug Delivery, Springer Singapore, Singapore, 2022. https://doi.org/10.1007/978-981-16-4566-2.

[4] Y.F. Zheng, X.N. Gu, F. Witte, Biodegradable metals, Mater. Sci. Eng. R Reports 77 (2014) 1–34. https://doi.org/10.1016/j.mser.2014.01.001.

[5] P.P. Tan, H. Mohamad, A.S. Anasyida, Properties of Porous Magnesium Using Polymethyl Methacrylate (PMMA) as a Space Holder, J. Phys. Conf. Ser. 1082 (2018). https://doi.org/10.1088/1742-6596/1082/1/012063.

[6] Y. Yun, Z. Dong, D. Yang, M.J. Schulz, V.N. Shanov, S. Yarmolenko, Z. Xu, P. Kumta, C. Sfeir, Biodegradable Mg corrosion and osteoblast cell culture studies, Mater. Sci. Eng. C 29 (2009) 1814–1821. https://doi.org/10.1016/j.msec.2009.02.008.

[7] F. Witte, The history of biodegradable magnesium implants: A review, Acta Biomater. 6 (2010) 1680–1692. https://doi.org/10.1016/j.actbio.2010.02.028.

[8] S. Zhang, J. Li, Y. Song, C. Zhao, X. Zhang, C. Xie, Y. Zhang, H. Tao, Y. He, Y. Jiang, Y. Bian, In vitro degradation, hemolysis and MC3T3-E1 cell adhesion of biodegradable Mg–Zn alloy, Mater. Sci. Eng. C 29 (2009) 1907–1912. https://doi.org/10.1016/j.msec.2009.03.001.

[9] G. Song, S. Song, A Possible Biodegradable Magnesium Implant Material, Adv. Eng. Mater. 9 (2007) 298–302. https://doi.org/10.1002/adem.200600252.

[10] L. Tan, M. Gong, F. Zheng, B. Zhang, K. Yang, Study on compression behavior of porous magnesium used as bone tissue engineering scaffolds, Biomed. Mater. 4 (2009) 015016. https://doi.org/10.1088/1748-6041/4/1/015016.

[11] R. Willumeit, J. Fischer, F. Feyerabend, N. Hort, U. Bismayer, S. Heidrich, B. Mihailova, Chemical surface alteration of biodegradable magnesium exposed to corrosion media., Acta Biomater. 7 (2011) 2704–15. https://doi.org/10.1016/j.actbio.2011.03.004.

[12] X. Li, X. Liu, S. Wu, K.W.K. Yeung, Y. Zheng, P.K. Chu, Design of magnesium alloys with controllable degradation for

[DOI: 10.22068/ijmse.4603]

biomedical implants: From bulk to surface, Acta Biomater. 45 (2016) 2–30. https://doi.org/10.1016/j.actbio.2016.09.005.

[13] G. Eddy Jai Poinern, S. Brundavanam, D. Fawcett, Biomedical Magnesium Alloys: A Review of Material Properties, Surface Modifications and Potential as a Biodegradable Orthopaedic Implant, Am. J. Biomed. Eng. 2 (2013) 218–240. https://doi.org/10.5923/j.ajbe.20120206.02.

[14] S.K. Sharma, K.K. Saxena, V. Malik, K.A. Mohammed, C. Prakash, D. Buddhi, S. Dixit, Significance of Alloying Elements on the Mechanical Characteristics of Mg-Based Materials for Biomedical Applications, Crystals 12 (2022). https://doi.org/10.3390/cryst12081138.

[15] M.B. Kannan, S. Liyanaarachchi, Hybrid coating on a magnesium alloy for minimizing the localized degradation for load-bearing biodegradable mini-implant applications, Mater. Chem. Phys. 142 (2013) 350–354. https://doi.org/10.1016/j.matchemphys.2013.07.028.

[16] P. Krokhicheva, D. Shornikov, M. Savelyev, Development of the technology of obtaining the composite based on the "magnesium-bone substance" for biodegradable implants by the method of powder metallurgy, IOP Conf. Ser. Mater. Sci. Eng. 525 (2019) 012029. https://doi.org/10.1088/1757-899X/525/1/012029.

[17] S. Amukarimi, M. Mozafari, Biodegradable magnesium-based biomaterials: An overview of challenges and opportunities, MedComm 2 (2021) 123–144. https://doi.org/10.1002/mco2.59.

[18] H.R. Bakhsheshi-Rad, M.H. Idris, M.R. Abdul-Kadir, A. Ourdjini, M. Medraj, M. Daroonparvar, E. Hamzah, Mechanical and bio-corrosion properties of quaternary Mg–Ca–Mn–Zn alloys compared with binary Mg–Ca alloys, Mater. Des. 53 (2014) 283–292. https://doi.org/10.1016/j.matdes.2013.06.055.

[19] A. Zakiyuddin, K. Lee, Effect of a small addition of zinc and manganese to Mg–Ca based alloys on degradation behavior in physiological media, J. Alloys Compd. 629 (2015) 274–283. https://doi.org/10.1016/j.jallcom.2014.12.181.

[20] J. Fu, W. Du, K. Liu, X. Du, C. Zhao, H. Liang, A. Mansoor, S. Li, Z. Wang, Effect of the Ca2Mg6Zn3 Phase on the Corrosion Behavior of Biodegradable Mg-4.0Zn-0.2 Mn-xCa Alloys in Hank's Solution, Materials (Basel). 15 (2022) 2079. https://doi.org/10.3390/ma15062079.

[21] Z. Li, X. Gu, S. Lou, Y. Zheng, The development of binary Mg–Ca alloys for use as biodegradable materials within bone, Biomaterials 29 (2008) 1329–1344. https://doi.org/10.1016/j.biomaterials.2007.12.021.

[22] Y.N. Zhang, D. Kevorkov, J. Li, E. Essadiqi, M. Medraj, Determination of the solubility range and crystal structure of the Mg-rich ternary compound in the Ca-Mg-Zn system, Intermetallics 18 (2010) 2404–2411. https://doi.org/10.1016/j.intermet.2010.08.033.

[23] K. Hagihara, S. Shakudo, T. Tokunaga, T. Nakano, Development of Zn–Mg–Ca Biodegradable Dual-Phase Alloys, Metals (Basel). 13 (2023) 1095. https://doi.org/10.3390/met13061095.

[24] Y.N. Zhang, D. Kevorkov, F. Bridier, M. Medraj, Experimental study of the Ca-Mg-Zn system using diffusion couples and key alloys, Sci. Technol. Adv. Mater. 12 (2011). https://doi.org/10.1088/1468-6996/12/2/025003.

[25] B. Zhang, Y. Hou, X. Wang, Y. Wang, L. Geng, Mechanical properties, degradation performance and cytotoxicity of Mg–Zn–Ca biomedical alloys with different compositions, Mater. Sci. Eng. C 31 (2011) 1667–1673. https://doi.org/10.1016/j.msec.2011.07.015.

[26] E. Zhang, L. Yang, Microstructure, mechanical properties and bio-corrosion properties of Mg–Zn–Mn–Ca alloy for biomedical application, Mater. Sci. Eng. A 497 (2008) 111–118. https://doi.org/10.1016/j.msea.2008.06.019.

[27] H. Du, Z. Wei, X. Liu, E. Zhang, Effects of Zn on the microstructure, mechanical property and bio-corrosion property of Mg-3Ca alloys for biomedical application, Mater. Chem. Phys. 125 (2011) 568–575. https://doi.org/10.1016/j.matchemphys.2010.10.015.

[28] R. Schmid-Fetzer, A. Janz, J. Gröbner, M. Ohno, Aspects of Quality Assurance in a Thermodynamic Mg Alloy Database, Adv. Eng. Mater. 7 (2005) 1142–1149. https://doi.org/10.1002/adem.200500175.

[29] C.L.L.C. Copyright, PandatTM 2023 Database Manual, (2023).

[30] M. Ghorbani, M. Boley, P.N.H. Nakashima,

[DOI: 10.22068/ijmse.4603]

N. Birbilis, A machine learning approach for accelerated design of magnesium alloys. Part A: Alloy data and property space, J. Magnes. Alloy. 11 (2023) 3620–3633. https://doi.org/10.1016/j.jma.2023.09.035.

[31] I. Morgenthal, O. Andersen, C. Kostmann, G. Stephani, T. Studnitzky, F. Witte, B. Kieback, Highly Porous Magnesium Alloy Structures and Their Properties Regarding Degradable Implant Application, Adv. Eng. Mater. 16 (2014) 309–318. https://doi.org/10.1002/adem.201300130.

[32] P. Holweg, L. Berger, M. Cihova, N. Donohue, B. Clement, U. Schwarze, N.G. Sommer, G. Hohenberger, J.J.J.P. van den Beucken, F. Seibert, A. Leithner, J.F. Löffler, A.-M. Weinberg, A lean magnesium-zinc-calcium alloy ZX00 used for bone fracture stabilization in a large growing-animal model., Acta Biomater. 113 (2020) 646–659. https://doi.org/10.1016/j.actbio.2020.06.013.

[33] Y.Z. Du, M.Y. Zheng, C. Xu, X.G. Qiao, K. Wu, X.D. Liu, G.J. Wang, X.Y. Lv, Microstructures and mechanical properties of as-cast and as-extruded Mg-4.50Zn-1.13Ca (wt%) alloys, Mater. Sci. Eng. A 576 (2013) 6–13. https://doi.org/10.1016/j.msea.2013.03.034.

[34] P. Gunde, A.C. Hänzi, A.S. Sologubenko, P.J. Uggowitzer, High-strength magnesium alloys for degradable implant applications, Mater. Sci. Eng. A 528 (2011) 1047–1054. https://doi.org/10.1016/j.msea.2010.09.068.

[35] S.H. Park, Y.J. Kim, H.J. Kim, S.-C. Jin, J.U. Lee, A. Komissarov, K.S. Shin, Recent research progress on magnesium alloys in Korea: A review, J. Magnes. Alloy. 11 (2023) 3545–3584. https://doi.org/10.1016/j.jma.2023.08.007.

[36] J. Hofstetter, M. Becker, E. Martinelli, A.M. Weinberg, B. Mingler, H. Kilian, S. Pogatscher, P.J. Uggowitzer, J.F. Löffler, High-Strength Low-Alloy (HSLA) Mg–Zn–Ca Alloys with Excellent Biodegradation Performance, JOM 66 (2014) 566–572. https://doi.org/10.1007/s11837-014-0875-5.

[37] J. Gröbner, R. Schmid-Fetzer, Key Issues in a Thermodynamic Mg Alloy Database, Metall. Mater. Trans. A 44 (2013) 2918–2934. https://doi.org/10.1007/s11661-012-1483-z.

[38] S. Wasiur-Rahman, M. Medraj, Critical assessment and thermodynamic modeling of the binary Mg–Zn, Ca–Zn and ternary Mg–Ca–Zn systems, Intermetallics 17 (2009) 847–864. https://doi.org/10.1016/j.intermet.2009.03.014.

[39] C.O. Brubaker, Z.-K. Liu, A computational thermodynamic model of the Ca–Mg–Zn system, J. Alloys Compd. 370 (2004) 114–122. https://doi.org/10.1016/j.jallcom.2003.08.097.

[40] M.-C.Z. Alloy, P.M. Jardim, G. Solórzano, J.B. Vander Sande, Precipitate Crystal Structure Determination in Melt Spun Mg-1.5wt% Ca-6wt%Zn Alloy, Microsc. Microanal. 8 (2002) 487–496. https://doi.org/10.1017/S1431927602010413.

[41] P. Mao, B. Yu, Z. Liu, F. Wang, Y. Ju, First-principles calculations of structural, elastic and electronic properties of AB2 type intermetallics in Mg–Zn–Ca–Cu alloy, J. Magnes. Alloy. 1 (2013) 256–262. https://doi.org/10.1016/j.jma.2013.10.001.

[42] Y. Kojima, Platform Science and Technology for Advanced Magnesium Alloys, Mater. Sci. Forum 350–351 (2000) 3–18. https://doi.org/https://doi.org/10.4028/www.scientific.net/MSF.350-351.3.

[43] P. Villars, K. Cenzual, eds., Mg Crystal Structure: Datasheet from "PAULING FILE Multinaries Edition-2022" in SpringerMaterials (https://materials.springer.com/isp/crystallographic/docs/sd{_}0456909), (n.d.). https://materials.springer.com/isp/crystallographic/docs/sd_0456909.

[44] P. Villars, K. Cenzual, eds., Mg Crystal Structure: Datasheet from "PAULING FILE Multinaries Edition–2022" in SpringerMaterials (https://materials.springer.com/isp/crystallographic/docs/sd_1933226), (n.d.). https://materials.springer.com/isp/crystallographic/docs/sd_1933226.

[45] R.E. Schäublin, M. Becker, M. Cihova, S.S.A. Gerstl, D. Deiana, C. Hébert, S. Pogatscher, P.J. Uggowitzer, J.F. Löffler, Precipitation in lean Mg–Zn–Ca alloys, Acta Mater. 239 (2022) 118223. https://doi.org/10.1016/j.actamat.2022.118223.

[46] P. Doležal, J. Zapletal, S. Fintová, Z. Trojanová, M. Greger, P. Roupcová, T. Podrábský, Influence of Processing Techniques on Microstructure and Mechanical Properties of a Biodegradable Mg-3Zn-2Ca Alloy, Materials (Basel). 9 (2016) 880. https://doi.

[DOI: 10.22068/ijmse.4603]

org/10.3390/ma9110880.
[47] H. Ibrahim, Bioresorbable Magnesium-Based Bone Fixation Hardware: Alloy Design, Post- Fabrication Heat Treatment, Coating, and Modeling, 2017. https://doi.org/15036 78544356525.
[48] P.-R. Cha, H.-S. Han, G.-F. Yang, Y.-C. Kim, K.-H. Hong, S.-C. Lee, J.-Y. Jung, J.-P. Ahn, Y.-Y. Kim, S.-Y. Cho, J.Y. Byun, K.-S. Lee, S.-J. Yang, H.-K. Seok, Biodegradability engineering of biodegradable Mg alloys: Tailoring the electrochemical properties and microstructure of constituent phases, Sci. Rep. 3 (2013) 2367. https://doi.org/10.1038/srep02367.
[49] K. Nie, Z. Zhu, P. Munroe, K. Deng, J. Han, The effect of Zn/Ca ratio on the microstructure, texture and mechanical properties of dilute Mg–Zn–Ca–Mn alloys that exhibit superior strength, J. Mater. Sci. 55 (2020) 3588–3604. https://doi.org/10.1007/s10853-019-04174-4.
[50] Y. Mingbo, G. Tingzhang, L. Hongliang, D. Chengyu, Z. Jia, Effects of Sn Addition on as-Cast Microstructure and Mechanical Properties of Mg-3.8Zn-2.2Ca Magnesium Alloy, Rare Met. Mater. Eng. 42 (2013) 1541–1546. https://doi.org/10.1016/S1875-5372(13)60086-7.
[51] G. Zhu, S. Lyu, G. Shen, L. Tian, M. Chen, Effect of the microstructure parameters on the mechanical properties and corrosion behavior of Mg alloys with high Zn or Ca content, J. Mater. Sci. 58 (2023) 12373–12390. https://doi.org/10.1007/s10853-023-08533-0.
[52] A. Gungor, A. Incesu, Effects of alloying elements and thermomechanical process on the mechanical and corrosion properties of biodegradable Mg alloys, J. Magnes. Alloy. 9 (2021) 241–253. https://doi.org/10.1016/j.jma.2020.09.009.
[53] N. Pulido-González, B. Torres, S. García-Rodríguez, P. Rodrigo, V. Bonache, P. Hidalgo-Manrique, M. Mohedano, J. Rams, Mg–1Zn–1Ca alloy for biomedical applications. Influence of the secondary phases on the mechanical and corrosion behaviour, J. Alloys Compd. 831 (2020) 154735. https://doi.org/10.1016/j.jallcom.2020.154735.
[54] D. Zander, P. Zaslansky, N.A. Zumdick, M. Felten, C. Schnatterer, V.F. Chaineux, J.U. Hammel, M. Storm, F. Wilde, C. Fleck, The Effect of Chemistry and 3D Microstructural Architecture on Corrosion of Biodegradable Mg–Ca–Zn Alloys, Adv. Eng. Mater. 23 (2021). https://doi.org/10.1002/adem.202100157.
[55] P. Yin, N. Feng, L. Ting, Effects of Ca on microstructure, mechanical and corrosion properties and biocompatibility of Mg–Zn–Ca alloys, J. Mater. Sci. Mater. Med. 24 (2013) 1365–1373. https://doi.org/10.1007/s10856-013-4856-y.
[56] W. Mueller, M.L. Nascimento, M. Fernández, L. De Mele, Critical discussion of the results from different corrosion studies of Mg and Mg alloys for biomaterial applications, Acta Biomater. 6 (2010) 1749–1755. https://doi.org/10.1016/j.actbio.2009.12.048.
[57] Z. Gui, Z. Kang, Y. Li, Corrosion mechanism of the as-cast and as-extruded biodegradable Mg-3.0Gd-2.7Zn-0.4Zr-0.1Mn alloys, Mater. Sci. Eng. C 96 (2019) 831–840. https://doi.org/10.1016/j.msec.2018.11.037.
[58] M.S. Ummah, CRC Handbook of Chemistry and Physics: A Ready-Reference of Chemical and Physical Data, 85th ed Edited by David R. Lide (National Institute of Standards and Technology). CRC Press LLC: Boca Raton, FL. 2004. 2712 pp. $139.99. ISBN 0-8493-0485-7., J. Am. Chem. Soc. 127 (2005) 4542–4542. https://doi.org/10.1021/ja041017a.
[59] A. Kucharczyk, K. Naplocha, J.W. Kaczmar, H. Dieringa, K.U. Kainer, Current Status and Recent Developments in Porous Magnesium Fabrication, Adv. Eng. Mater. 20 (2018) 1–16. https://doi.org/10.1002/adem.201700562.
[60] Z. Shi, M. Liu, A. Atrens, Measurement of the corrosion rate of magnesium alloys using Tafel extrapolation, Corros. Sci. 52 (2010) 579–588. https://doi.org/10.1016/j.corsci.2009.10.016.
[61] ASTM, Standard Guide for in vitro Degradation Testing of Absorbable Metals, ASTM Int. F3268−18 (2018) 1–13. https://doi.org/10.1520/F3268-18A.1.8.
[62] D. Zander, N.A. Zumdick, Influence of Ca and Zn on the microstructure and corrosion of biodegradable Mg-Ca-Zn alloys, Corros. Sci. 93 (2015) 222–233. https://doi.org/10.1016/j.corsci.2015.01.027.
[63] Y. Lu, A.R. Bradshaw, Y.L. Chiu, I.P. Jones, Effects of secondary phase and grain size on the corrosion of biodegradable Mg–Zn–

[DOI: 10.22068/ijmse.4603]

Ca alloys, 48 (2015) 480–486. https://doi.org/10.1016/j.msec.2014.12.049.

[64] Y. Jang, Z. Tan, C. Jurey, Z. Xu, Z. Dong, B. Collins, Y. Yun, J. Sankar, Understanding corrosion behavior of Mg–Zn–Ca alloys from subcutaneous mouse model : Effect of Zn element concentration and plasma electrolytic oxidation, Mater. Sci. Eng. C 48 (2015) 28–40. https://doi.org/10.1016/j.msec.2014.11.029.

[65] G. Derringer, R. Suich, Simultaneous Optimization of Several Response Variables, J. Qual. Technol. 12 (1980) 214–219. https://doi.org/10.1080/00224065.1980.11980968.

[66] K. Hagihara, S. Shakudo, K. Fujii, T. Nakano, Degradation behavior of Ca-Mg-Zn intermetallic compounds for use as biodegradable implant materials., Mater. Sci. Eng. C. Mater. Biol. Appl. 44 (2014) 285–92. https://doi.org/10.1016/j.msec.2014.08.037.

[DOI: 10.22068/ijmse.4603]